Check for updates

Vortex mediated fabrication of 2D antimonene sheets from antimony powder†

Fayed Abdullah Alrashaidi,[ab] Soraya Rahpeima,[ac] Xuan Luo, [ID] [a] Kasturi Vimalanathan, [ID] [a] Abdulrahman S. Alotabi, [ID] [ad] Thaar Alharbi,[e] Xianjue Chen,[f] Dechao Chen, [ID] [g] Youhong Tang, [ID] [a] Christopher Gibson,[ah] Nadim Darwish,[c] Qin Li [ID] [g] and Colin L. Raston [ID] *[a]

Antimony powder is transformed into 2D antimonene in a vortex fluidic device (VFD) at ambient conditions, depending on the choice of solvent (optimised as a 1 : 1 mixture of isopropyl alcohol and dimethylformamide) and the operating parameters of the microfluidic platform which houses a rapidly rotating quartz tube inclined at +45°. It is hypothesised that the Coriolis force from the hemispherical base of the tube, as typhoon like high-shear topological fluid flow down to submicron dimensions, generates localised heating at the quartz interface. This melts the antimony powder (m.p. 630.6 °C) *in situ* which crystallizes in the β-phase, with semi-conducting antimonene a few layers thick, and demonstrating novel photoluminescence.

The first 2D nanomaterial (NMs) discovered was graphene, in 2004,[1] with now numerous other 2D materials restricted in one direction being reported.[2,3] 2D NMs have attracted significant interest owing to their unique chemical and physical properties. These properties are important in catalysis, energy storage, sensors, and electronic devices.[4] 2D NMs include hexagonal boron nitride,[5] silicene,[6] and germanene[7] of the group 14 elements, as for carbon. Group 15 elements (pnictogens) can also form 2D NMs, as arsenene, phosphorene[8] and antimonene[9] with the latter having potential in thermal energy conversion, optoelectronics, spintronics, and electronics.[4] Enhanced stability, high carrier mobility, and a tuneable bandgap are only some of the novel properties of antimonene.[10]

A variety of approaches have been developed for the synthesis of antimonene, with first-principal calculations predicting that it has a stable 2D β-phase with unique properties, with its specific synthesis challenging.[11–13] The synthesis of 2D NMs in general involves top-down and bottom up[14] approaches with the latter involving chemical vapour deposition (CVD),[15] epitaxial growth, and wet-chemical synthesis.[16] Top-down approaches include mechanical exfoliation, sonication-assisted solvent exfoliation, and liquid-phase exfoliation (LPE).[17,18] The synthesis of high quality 2D antimonene as a top down process is challenging because of the stronger interlayer binding between individual sheets.[9] Sb has a high melting point (630.6 °C) which would normally preclude solution-based recrystallisation of the element as a route to producing nano-materials, including any subsequent exfoliation requirements for generating antimonene. We now report the direct synthesis of 2D antimonene from elemental Sb powder in organic solvents in a vortex fluidic device (VFD),[19] Fig. 1(a), using short processing times (10 min) and without the need for using auxiliary substances. The VFD is a thin film microfluidic platform housing a rapidly rotating quartz tube with a hemispherical base, tilted at 45° (θ) which is optimal for most applications.[20,21] Mechanical energy is induced in localised micron/submicron heating regimes[22,23] at the interface of the quartz tube and the liquid thin film which remarkably melts Sb *in situ*, crystallising into multi-layered antimonene. These heating regimes are formed by Coriolis force generated at the base of the tube as spinning top (ST) (typhoon like) high-shear topological fluid flows, Fig. 1(a).[24,25] Melting as such in an organic solvent in the VFD has been achieved at room temperature for bismuth (271.4 °C).[22] It is also noteworthy that global changes in temperature in the VFD during processing are

aFlinders Institute for Nanoscale Science and Technology, College of Science and Engineering, Flinders University, Adelaide, SA 5042, Australia. E-mail: colin.raston@flinders.edu.aus

bDepartment of Chemistry, College of Science, Jouf University, Sakaka 72388, Saudi Arabia

cSchool of Molecular and Life Sciences, Curtin Institute for Functional Molecule and Interfaces, Curtin University, Bentley, Western Australia 6102, Australia

dDepartment of Physics, Faculty of Science, Al-Baha University, Al-Baha 65779, Saudi Arabia

ePhysics Department, Faculty of Science, Taibah University, Almadinah, Almunawwarrah 42353, Saudi Arabia

fSchool of Environmental and Life Sciences, The University of Newcastle, Callaghan, New South Wales 2308, Australia

gQueensland Micro- and Nanotechnology Centre, Griffith University, Brisbane, QLD 4111, Australia

hFlinders Microscopy and Microanalysis, College of Science and Engineering, Flinders University, Adelaide, SA 5042, Australia
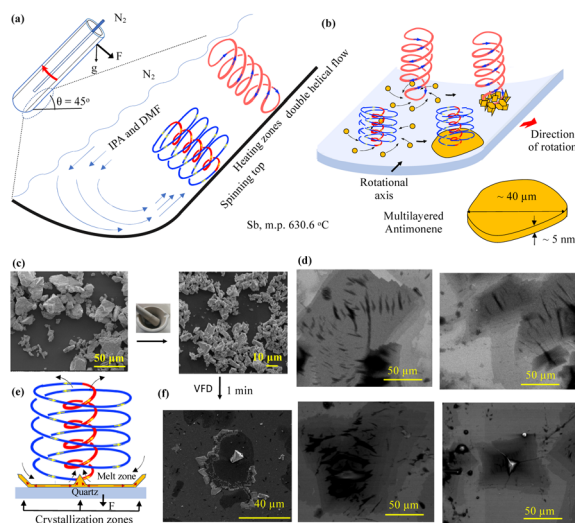
Fig. 1 Schematic diagram showing the VFD operating in the confined mode under N_2 gas and the high-shear topological fluid flows of micron/submicron dimensions, (a), for converting Sb powder into 2D antimonene, at the base of the spinning top topological flow, (b). (c) SEM images of as-received Sb powder and the powder ground to smaller particles, for then processing in the VFD in a mixture of IPA and DMF (optimised), concentration 0.25 mg mL^{-1}, θ 45°, ω 4.5k rpm, 10 min processing at ambient temperature. (d) SEM images of the resulting antimonene. (e) Proposed mechanism of the shear stress-induced melting and crystallisation of Sb, supported by (f) SEM images of a crater of Sb formed after 5 min processing in water, under N_2 gas, under UV 254 nm, 0.25 mg mL^{-1}, θ 45°, ω 4.5k rpm (see also Fig. S3(a)†).

minimal with high heat dissipation and the ability to carry out highly exothermic reactions at room temperature.[21]

The VFD has been used to specifically exfoliate 2D materials, including graphite,[26] boron nitride,[26] phosphorene,[27] MXene,[28] and MoS_2.[29] However, for the purpose of preparing antimonene herein, the primary effect of the VFD is localised shear stress-induced melting and recrystallization from ST flow, rather than direct exfoliation, and the processing is therefore distinctly different. We note that for either topological fluid flows, Fig. 1(a), periodically there will be areas where shear stress on the surface of the tube is minimal, as established from 'molecular drilling' experiments for polymer films deposited on the surface of the tube.[23] In these areas, dense antimony particles are expected to be held centrifugally against the surface of the tube. This will position them for the approaching high shear flows moving across the surface of the tube, for then melting of the antimony within ST flow, in forming thin sheets of the element. Single high shear exposure events as such are expected to be short, noting that enzymatic reaction rates are dramatically enhanced in the VFD without the enzymes being degraded under otherwise compromising conditions.[20,21]

The as-received bulk Sb powder was pulverised in air for 10 min in a mortar and pestle, affording 5 to 50 μm particles, Fig. 1(c), followed by dispersing 5 mg of the finely divided material in 20 mL IPA and DMF in a 1 : 1 ratio, which was optimal for confined mode processing (see below) or similarly for other solvents systems, and also water, although here for

long processing times, there is extensive oxidation, ESI Fig. S2.† Next, 1 mL of this liquid was placed into a 20 mm diameter quartz VFD tube (17.5 mm internal diameter (ID)) 18.5 mm in length, and was then processed under dry N_2 gas in order to minimise any oxidation of Sb, as evident in Fig. S1† with charging of the particles apparent in the SEM images. The tube was spun at 4.5k rpm for which the ST is the dominant topological flow,[22] and for which we hypothesised that the localised heating would melt the element. This type of processing is the so-called confined mode of operation of the VFD, and for larger scale synthesis we used the up-sized large VFD (L-VFD) which houses a 50 mm OD (46 mm ID) quartz tube, 45 cm in length (see below).[30] The corresponding speed here for the dominant ST flow is 1.75k rpm, with the volume capacity of liquid in the tube ~30 mL. This is in contrast to a maximum of 2 mL for the 20 mm diameter tube rotating at 4.5k rpm.[30] For all processing in both diameter tubes, the tilt angle θ was set at +45°.

The effect of different concentrations of Sb powder on the formation of 2D antimonene (0.1, 0.25, 1, 3, 5 and 10 mg mL^{-1}) (ESI Fig. S3 and S4†), was also investigated, with 3 mg.mL^{-1} giving the highest isolated yield, at 16%. This intermediate concentration most likely represents the highest concentration before the particles of the starting material begin to disturb the topological fluid flow, as noted in other materials applications of the VFD.[20,21] After processing in the VFD (20 mm OD tube), all mixtures were centrifuged for 5 min at 1200×g to precipitate any unprocessed Sb particles which can be recycled. The supernatant was then drop cast onto a Si wafer for SEM, Raman spectroscopy, AFM, and XPS studies. SEM images showed the formation of flat sheets, Fig. 1(d).

SEM images of material generated from antimony powder after short processing times in the VFD provided insight into the mechanism of formation of the antimonene. Some 2D sheets are formed after 30 s processing, with increasing conversion for increasing processing times, Fig. S1(d–i), S4(a and b)†; 5 min processing revealed craters with a central ridge, Fig. 1(f), which represent a mould of the base of the ST flow with the ridge arising from rapid cooling and crystallisation as the liquid antimony is drawn up the ST and rapidly cooled, noting the high heat transfer to the surrounding liquid in the dynamic thin film of solvent. The above central ridges were initially formed under UV radiation ($\lambda = 254$ nm) in studying field effects for the processing for which the VFD is highly adaptable.[20,21] However, there was no apparent effect with central ridges identified in the absence of UV, Fig. S3(a).†

The melting occurs at the interface of the liquid and the surface of the tube with the pressure of the fluid flow down on the surface of the tube ensuring that the thickness of the Sb is minimal. Added to this, the lateral sideways force in the ST can induce exfoliation of the Sb post squeezing, into a thin layer of the element, as established for MoS_2 exfoliation.[29] VFD processing transforms the chunky antimony particles ~5 to 50 μm in diameter into sheets with lateral dimensions ~80 to 115 μm, for 0.25 mg.mL^{-1} concentration of Sb, Fig. 1(d). This was determined from SEM images, using ImageJ for 23 particles for each sample, Fig. S3(e–g).† The lateral dimensions of the processed Sb are much larger than that of the starting material with

their thickness investigated using AFM, Fig. 2. Height profile experiments establishes that the sheets are ~3 and 5 nm thick. The approximate volume of these thin sheets (~115 μm × 80 μm × ~5 nm), ESI Fig. S3(C),† is 46 μm³ which is consistent with it being derived from a single particle of starting material. Processing for 30 s and 2 min affording 2D sheets 16 to 126 nm thick, ESI Fig. S4(a, b) and S9.† This is also consistent with the ST topological fluid flow rapidly heating Sb particles on the interfacial surfaces of VFD tubes to ultimately form very thin antimonene sheets. Raman spectroscopy is applicable for Sb,[31] and for the bulk material used in the present study, the Eg and A1g modes of vibration are at 110 and 146 cm^{-1}, respectively (λ = 532 nm). However, no Raman signal was evident for the generated antimonene, ESI Fig. S5(a),† as noted previously for ultrathin material of Sb.[32,33]

CoK$_\alpha$ X-ray diffraction (XRD) established that the as-received and transformed thin sheets correspond to the β-phase of Sb, Fig. 3(a). The intensity of the c-axis plane (003), $2\theta = 27.63°$, and the second harmonic plane at 56.93° (006) is consistent with the formation of thin sheets of Sb. The X-ray diffraction (XRD) data establishes that the as-received antimony, which according to the standard card (JCPDS No. 00-035-0732) is the hexagonal phase, is transformed into exclusively thin sheets of the β-Sb phase, Fig. 3(a and b), with no peak evident for the 2θ peak corresponding to the (003) plane at $2\theta = 27.63°$ in the VFD prepared 2D antimonene, Fig. 3(a). In addition, the highest peak corresponding to the (012) plane is shifted from $2\theta = 33.50°$ for the as received Sb to 33.60° for the 2D material, Fig. 3(b), which is due to lattice shrinkage.[31,34]

High resolution (HR)-TEM images with a d spacing of 0.22–0.23 nm and Fast Fourier transform (FFT) images match the β-phase for the antimonene, Fig. 3(c–f),[12,34] with no noticeable defects, with EDX mapping and sum spectra of TEM-EDX mapping in Fig. 3(g) and ESI S8,† respectively. The X-ray photoelectron spectroscopy (XPS) survey spectra of Sb powder and Sb sheets, Fig. 4(a and b), show the core level spectrum of Sb 3d with doublet peaks at 529.8 and 539 eV, corresponding to Sb 3d$_{5/2}$ and Sb 3d$_{3/2}$, which are shifted to 530 and 539.5 eV due to Sb–O moieties, ESI Fig. S6.† The Sb 3d$_{3/2}$ and Sb 3d$_{5/2}$ peaks overlap with an O 1s peak at 530.3 eV, and also noteworthy is a N 1s peak and a C 1s peak, presumably arising from solvent molecules coordinating to Sb. The presence of oxygen can arise from some oxidation of Sb and/or the presence of IPA/DMF physisorbed or covalently attached through oxygen as coordination interactions, or indeed decomposition of the solvents. For the latter, we note that antimonene can be covalently
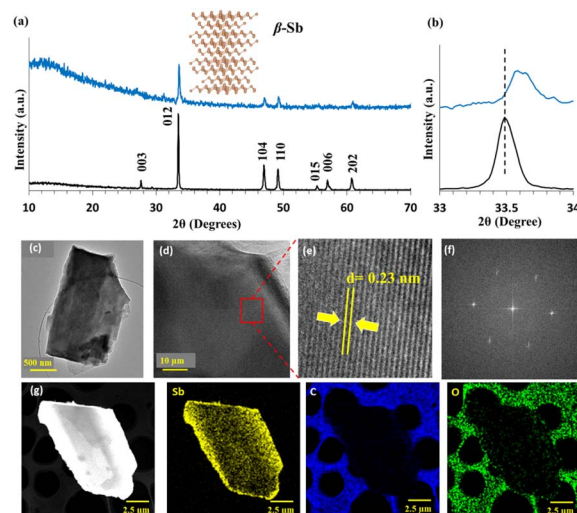

Fig. 3 (a) XRD for as-received (black) and VFD-processed Sb (blue) using optimal conditions (λ 1.79 Å), along with the structure of the β-phase, Fig. 1. (b) Broadened and shifted (012) peaks for processed material (blue) relative to as-received Sb (back). (c) TEM image of 2D Sb sheets. (d) HR-TEM with zoom section in (e) for interplanar spacing. (f) Fast Fourier Transform (FFT) pattern from (c). (g) EDX elemental mapping of material formed under the optimised conditions in Fig. 1.

functionalized,[35] forming stable coordination bonds, thereby protecting and shielding the antimony surface from oxidation and environmental degradation. Thermogravimetric analysis (TGA) showed ~50% weight loss up to 420 °C, mostly above ~200 °C, with gradual weight loss leading up to 600 °C, with differential scanning calorimetry (DSC) showing no phase change, Fig. 4(c). A further 4.08% loss of mass occurred between 420 and 500 °C, and 6.2% between 500 and 600 °C, which suggests that any surface bound moieties have been removed. After heating the sample to 600 °C, XRD of the cooled sample, ESI Fig. S7,† revealed two new peaks assignable to the presence of Sb$_2$O$_3$ (ref. 36) ($2\theta = 37.5°$ and 53.5°) which could arise from surface oxidation of elemental Sb on exposure to air after TGA analysis and/or decomposition of physisorbed IPA.

We investigated the scaling up of the synthesis of antimonene initially under continuous flow which involved delivering a 0.25 mg mL^{-1} solution to the base of the VFD tube at 0.5 mL min^{-1} using a syringe pump, ω = 4.5k rpm and θ = 45°. However, the material adhered to the side wall of the tube, and interestingly tilting the tube to θ = −45° (top of the tube below the horizontal position) under continuous flow resulted in the formation of irregular rods rather than 2D material. This tilt angle has been used for exfoliating 2D h-BN[5] under flow, and the formation of the rods herein at this tilt angle establishes that the high shear under these conditions also melts the Sb. In addition, the results are consistent with the presence of ST flow originating from the base of the tube for θ = 45° as the primary force for generating the antimonene sheets with any exfoliation as a secondary process, Fig. S3(d)†.[37] We also used a L-VFD with θ = 45° and ω = 1.6k and 1.8k rpm, ESI Fig. S4(d–f),† noting that 4.5k rpm for the 20 mm diameter VFD corresponds to 1.75k rpm for the L-VFD in terms of shear stress effects.[23,30]
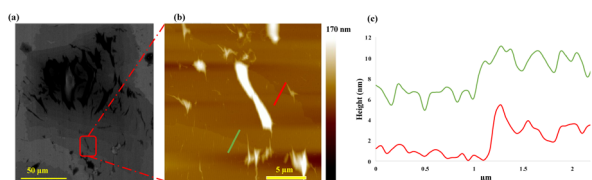

Fig. 2 (a) SEM and (b) AFM images of antimoene with (c) height profiles for the indicated positions, with the sample prepared using optimal conditions, Fig. 1.
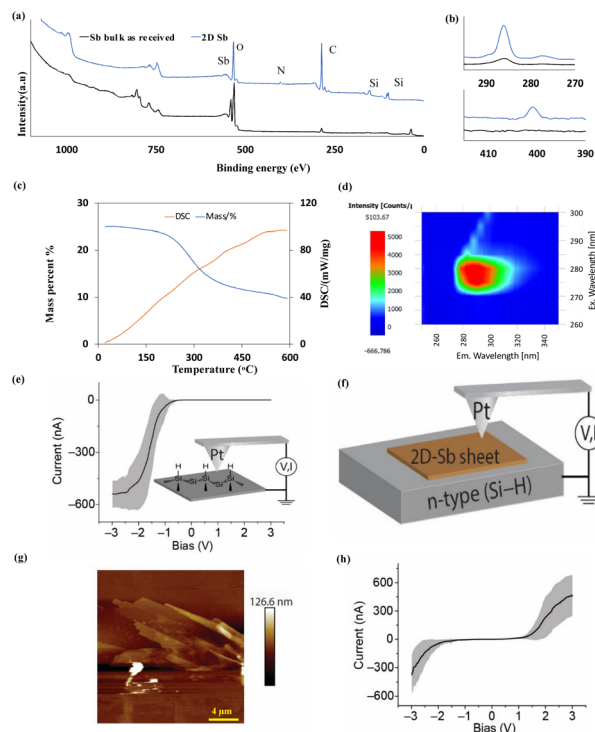
© 2024 The Author(s). Published by the Royal Society of Chemistry

Fig. 4 (a) XPS survey of as-received Sb and antimonene sheets formed in IPA: DMF in the VFD operating in the confined mode for the optimised conditions in Fig. 1. (b) Zoomed in C and N peaks. (c) TGA and DSC curves for the 2D Sb sheets heated under N_2 gas at 10 °C min^{-1}. (d) Excitation emission matrix of the 2D Sb sheets. (e) Current–voltage ($I–V$) measurement for (Si–H)–Pt junction showing the typical current rectifying behaviour of a metal–semiconductor junction. Inset in (e) shows a schematic of the AFM ($I–V$) measurement for (Si–H)–Pt junction. (f) Schematic of AFM ($I–V$) measurement for (Si–H)–Sb–Pt junction. (g) AFM height topography of (Si–H)–Sb sheets–Pt junction. (h) ($I–V$) measurements corresponding to the 2D-Sb sheet shown in AFM image in (g) that formed under optimal conditions in Fig. 1.

Here the use of a higher concentration of Sb of 10 mg mL^{-1} was possible in forming antimonene of comparable thickness to that of processing in L-VFD, ESI Fig. S4(d–f)† with 26.7 mg of the material isolated (13.5%) after 10 min processing of 20 mL of solution in the confined mode; continuous flow processing using the L-VFD was not possible for the same reason as for the 20 mm diameter tube.

UV absorption for the antimonene occurs at 230 nm, showing photoluminescence (PL) properties ranging from 280 to 320 nm, Fig. 4(d), for the material synthesised in the L-VFD, for a concentration of 10 mg mL^{-1}. To our knowledge, there is no report that the absorption of 2D antimonene in specific UVB regions. Through the Tauc plot, ESI Fig. S10,† the bandgap of this antimonene nanodisc is determined to be 4.87 eV, as the first wide bandgap for antimonene, and is likely due to the quantum confinement effect. This finding provides evidence for a strategy for tuning the emission properties of 2D antimonene sheets, using VFD processing, and offering a way for its potential application as a light-source material and in other areas which are requiring the emission of light in this region.

Current–voltage measurements of the broad antimonene sheets was acquired using conductive atomic force microscopy (CAFM) involving sandwiching the 2D Sb sheets between a Pt AFM-tip and a Si surface under a bias voltage, Fig. 4(e and f). Unlike direct Pt–Si circuits that show asymmetrical current–voltage properties (rectifier), the Pt-2D-Sb-sheet-Si junctions, Fig. 4(g and h), illustrates relatively more symmetrical current–voltage plots typical of ohmic contacts. These results have implications in nanoelectronics since Sb is often used for Si doping , ESI Fig. S11.†

2D Antimonene sheets are accessible directly from bulk Sb particles a few microns in diameter, using VFD-processing carried out at ambient temperature without the additional of auxiliary agents. Optimal conditions were derived by systematically exploring the VFD parameter space, and the choice of solvent mixture, in the confined mode, with then translating to the upsized larger tube. The spinning top Coriolis generated by the hemispherical base of the tube imparts the mechanical energy to melt the Sb and then squeeze it into a thin film, which crystallises as a 2D material composed of a few layers of antimonene in the β-phase, 3 to 5 nm thick. The exclusively formed β-phase antimonene sheets are thermally stable and behave as wide bandgap semiconductors with unique photoluminescence properties.

Data availability

The data supporting this article have been included as part of the ESI.†

Conflicts of interest

There are no conflicts to declare.

Acknowledgements

References

1 H. Tang, C. M. Hessel, J. Wang, N. Yang, R. Yu, H. Zhao and D. Wang, *Chem. Soc. Rev.*, 2014, **43**, 4281–4299.
2 J.-y. Kim, X. Ju, K.-W. Ang and D. Chi, *ACS Nano*, 2023, **17**(3), 1831–1844.
3 J. Li, Y. Li, Y. Lu, Y. Wang, Y. Guo and W. Shi, *Biomimetics*, 2023, **8**, 35.

4 S. B. Mujib, Z. Ren, S. Mukherjee, D. M. Soares and G. Singh, *Adv. Mater.*, 2020, **1**(8), 2562–2591.

5 A. H. M. Al-Antaki, X. Luo, T. M. Alharbi, D. P. Harvey, S. Pye, J. Zou, W. Lawrance and C. L. Raston, *RSC Adv.*, 2019, **9**, 22074–22079.

6 H. Lin, W. Qiu, J. Liu, L. Yu, S. Gao, H. Yao, Y. Chen and J. Shi, *Adv. Mater.*, 2019, 1903013.

7 K.-C. Chen, L.-M. Lee, H.-A. Chen, H. Sun, C.-L. Wu, H.-A. Chen, K.-B. Lin, Y.-C. Tseng, C.-C. Kaun and C.-W. Pao, *Semicond. Sci. Technol.*, 2019, **34**, 105020.

8 M. A. Tapia, R. Gusmao, N. Serrano, Z. Sofer, C. Ariño, J. M. Díaz-Cruz and M. Esteban, *TrAC, Trends Anal. Chem.*, 2021, **139**, 116249.

9 X. Wang, J. Song and J. Qu, *Angew. Chem., Int. Ed.*, 2019, **58**, 1574–1584.

10 L. Zhang, S. Fahad, H.-R. Wu, T.-T. Dong, Z.-Z. Chen, Z.-Q. Zhang, R.-T. Liu, X.-P. Zhai, X.-Y. Li and X. Fei, *Nanoscale Horiz.*, 2020, **5**, 1420–1429.

11 X. Wang, X. Yu, J. Song, W. Huang, Y. Xiang, X. Dai and H. Zhang, *Chem. Eng. J.*, 2021, **406**, 126876.

12 J. Ji, X. Song, J. Liu, Z. Yan, C. Huo, S. Zhang, M. Su, L. Liao, W. Wang and Z. Ni, *Nat. Commun.*, 2016, **7**, 13352.

13 J. Li, K. Yu, X. Zhang, Y. Li, L. Qiao, X. Peng, X. Dong, Z. Wang, J. Ma, W. Xiao and Y. Yao, *J. Phys. Chem. C*, 2022, **126**(10), 5022–5027.

14 J. A. Carrasco, P. Congost-Escoin, M. Assebban and G. Abellán, *Chem. Soc. Rev.*, 2023, 1288–1330.

15 C. Murugan, V. Sharma, R. K. Murugan, G. Malaimegu and A. Sundaramurthy, *J. Contr. Release*, 2019, **299**, 1–20.

16 Q. Wu and Y. J. Song, *Chem. Commun.*, 2018, **54**, 9671–9674.

17 J. Zhang, S. Ye, Y. Sun, F. Zhou, J. Song and J. Qu, *Nanoscale*, 2020, **12**, 20945–20951.

18 C. Gibaja, D. Rodriguez-San-Miguel, P. Ares, J. Gómez-Herrero, M. Varela, R. Gillen, J. Maultzsch, F. Hauke, A. Hirsch and G. Abellán, *Angew. Chem.*, 2016, **128**, 14557–14561.

19 B. A. Grzybowski, Y. I. Sobolev, O. Cybulski and B. Mikulak-Klucznik, *Nat. Rev. Mater.*, 2022, **7**, 338–354.

20 J. Britton, K. A. Stubbs, G. A. Weiss and C. L. Raston, *Chem.–Eur. J.*, 2017, **23**, 13270–13278.

21 C. Chuah, X. Luo, J. Tavakoli, Y. Tang and C. L. Raston, *Aggregate*, 2024, e433.

22 T. M. Alharbi, *et al.*, *Nanoscale Adv.*, 2021, **3**, 3064–3075.

23 M. Jellicoe, *et al.*, *Chem. Sci.*, 2022, **13**, 3375–3385.

24 K. Vimalanathan, Z. Zhi, Z. Jin and C. L. Raston, *Chem. Commun.*, 2023, **59**(64), 9698–9701.

25 K. Vimalanathan, S. James, P. Xun, X. Luo, S. Rahpeima, Q. Sun, J. Zou, *et al.*, *Nanoscale Adv.*, 2022, **4**, 3121–3130.

26 X. Chen, J. F. Dobson and C. L. Raston, *Chem. Commun.*, 2012, **48**, 3703–3705.

27 M. Batmunkh, K. Vimalanathan, C. Wu, A. S. Bati, L. Yu, S. A. Tawfik, M. J. Ford, T. J. Macdonald, C. L. Raston and S. Priya, *Small Methods*, 2019, **3**, 1800521.

28 A. H. Mohammed Al-antaki, S. Kellici, N. P. Power, W. D. Lawrance and C. L. Raston, *R. Soc. Open Sci.*, 2020, **7**, 192255.

29 T. M. Alharbi, S. Elmas, A. S. Alotabi, M. R. Andersson and C. L. Raston, *ACS Sustain. Chem. Eng.*, 2022, **10**, 9325–9333.

30 S. He, K. Vimalanathan, P. Su, M. Jellicoe, X. Luo, W. Xing, W. Cai, C. T. Gibson, Y. Chen and J. W. C. Wong, *ACS Sustain. Chem. Eng.*, 2021, **9**, 14588–14595.

31 M. M. Ismail, J. Vigneshwaran, S. Arunbalaji, D. Mani, M. Arivanandhan, S. P. Jose and R. Jayavel, *Dalton Trans.*, 2020, **49**, 13717–13725.

32 P. Ares, J. J. Palacios, G. Abellán, J. Gómez-Herrero and F. Zamora, *Adv. Mater.*, 2018, **30**, 1703771.

33 P. Ares, F. Aguilar-Galindo, D. Rodríguez-San-Miguel, D. A. Aldave, S. Díaz-Tendero, M. Alcamí, F. Martín, J. Gómez-Herrero and F. Zamora, *Adv. Mater.*, 2016, **28**, 6332–6336.

34 L. Peng, S. Ye, J. Song and J. Qu, *Angew. Chem., Int. Ed.*, 2019, **58**, 9891–9896.

35 M. M. Ayyub, M. Barua, S. Acharya and C. N. R. Rao, *Small*, 2022, **18**, 2203554.

36 H. S. Chin, K. Y. Cheong and K. A. Razak, *J. Mater. Sci.*, 2010, **45**, 5993–6008.

37 A. H. M. Al-Antaki, X. Luo, T. M. Alharbi, D. P. Harvey, S. Pye, J. Zou, W. Lawrance and C. L. Raston, *RSC Adv.*, 2019, **9**, 22074–22079.